ORIGINAL ARTICLE

Variations in uniform hazard spectra and disaggregated scenarios during earthquake sequences

Alireza Azarbakht[1,2] ⓘ · John Douglas[1] ⓘ

Abstract

Seismic hazard varies greatly during an earthquake sequence. Understanding this variation can be useful to end-users, such as emergency managers, as it would enable them to make more informed decisions about potential risk reduction measures. This article presents examples of how two commonly-used products of probabilistic seismic hazard assessments: uniform hazard spectra and disaggregated earthquake scenarios, vary during two severe seismic sequences in western Greece. These calculations are made using a recent time-dependent seismic hazard model based on a Bayesian ETAS approach. The examples show that time-dependent uniform hazard spectra for short return periods (1 and 10 years) are significantly higher than standard time-independent spectra but that uniform hazard spectra for the commonly-used return periods of 475 and 2475 years are similar to those from time-independent assessments. The time-dependent spectra generally converge within a couple of days to the time-independent spectra. The examples also show that the dominant earthquake scenarios evidenced by the disaggregation for the time-dependent assessment can show significant differences from the time-independent scenarios. This is particularly true when the earthquake sequence is distant from the location of interest as the aftershocks contribute greatly to the overall hazard. To show these changes more clearly this article introduces a new graphical representation of the disaggregated results: contour maps showing the magnitude or distance of the dominant earthquake scenario with axes of the structural period and response spectral acceleration.

Keywords Time-dependent PSHA · Disaggregation · UHS · Seismic sequence · Dominant earthquake scenario · Greece

✉ Alireza Azarbakht
    A.Azarbakht@greenwich.ac.uk

    John Douglas
    john.douglas@strath.ac.uk

[1]   Department of Civil and Environmental Engineering, University of Strathclyde, James Weir
      Building 75 Montrose Street, Glasgow G1 1XJ, Scotland, UK

[2]   School of Engineering, University of Greenwich, Medway Campus, Chatham ME4 4TB, UK

1 Introduction

To improve the accuracy of structural response estimates, nonlinear dynamic analyses of structures are becoming increasingly recommended by seismic design codes and other regulatory documents (e.g. ASCE7-05 2005; CEN-Eurocode 2003). A key basis of these approaches is to target a specific seismic hazard level. The goal of this article is to estimate the changes in seismic hazard during periods when there is a higher chance of a large earthquake (e.g. during seismic sequences). The rate of increase above the background (time-invariant) hazard during aftershock periods is a function of both the time since the mainshock (delay) and the forecasting duration (Field and Milner 2018). A number of studies have been published that estimate how much the likelihood of a potentially-damaging earthquake increased during specific sequences. These estimates range from about 20 times (Marzocchi et al. 2015) to around 1,000 times (Gulia et al. 2016; McBride et al. 2020). Jordan and Jones (2010) pointed out that the USGS's short-term earthquake probability (STEP) model (Gerstenberger et al. 2005) frequently showed increases in probabilities of ground motions exceeding a Modified Mercalli Intensity of VI of 10 to 100 times. Gerstenberger et al. (2005) themselves showed a map with increases of up to 30 times in some parts of California. Before the mainshock on 30 October 2016 of the 2016–2017 Central Italy earthquake sequence, the weekly likelihood of intensity VII near Norcia was reported to have increased by roughly three orders of magnitude (Marzocchi et al. 2017); thus, increases in ground shaking probabilities can be very significant.

It is worth noting that this rapid increase in seismic hazard has been commonly referred to in the literature for the purposes of Operational Earthquake Forecasting (OEF). Nevertheless, despite the magnitude of these increases, the change in seismic hazard is not commonly considered in seismic risk assessment. The aim of this article is to better understand the potential changes to key outputs of probabilistic seismic hazard assessments (PSHAs), including uniform hazard spectra (UHS) and disaggregated earthquake scenarios. To do this, the increases in the time-independent probabilities obtained from a recent time-dependent hazard model, based on Bayesian-inference updating, by Azarbakht et al. (2022) are used, to investigate how UHS and disaggregated scenarios can change during a seismic sequence.

PSHA statistically aggregates all possible earthquake ground motions that could occur at a given location (Cornell 1968). Within PSHA, it is also possible to account for epistemic uncertainty using a set of ground motion prediction equations (GMPEs), different source models, and other seismicity characteristics. For a single seismic source, the most practical version of PSHA is (Cornell 1968; McGuire 1995):

$$\lambda(y) = \nu \iint f_M(m) f_R(r) P[Y > y | m, r] dm dr \tag{1}$$

where $\lambda(y)$ is the rate of occurrence of ground motions with an Intensity Measure (IM) > y. $f_M(m)$ and $f_R(r)$ are the probability density functions associated with magnitude (M) and distance (R), respectively. $P[Y > y | m, r]$ is derived from an appropriate GMPE and ν is the rate of occurrence of earthquakes larger than a minimum magnitude for the specific seismic source.

The (pseudo) spectral acceleration corresponding to the fundamental period of vibration of a particular structure and a chosen damping ratio, i.e. $Sa(T_1, 5\%)$, is the most commonly-used IM. Within Eq. (1), the disaggregation of seismic hazard can also be computed for a given probability of exceedance in order to determine the relative contribution of the

various earthquake scenarios (Bazzurro and Cornell, 1999). Disaggregation can be done for any collection of seismic parameters, such as M and R. The main benefit of disaggregation is to obtain the dominant scenario for a given site. In other words, the dominant M and R is the event that contributes most to the double integral of Eq. (1).

Another potential output of PSHA is a target design spectrum. As discussed above, in most design procedures, the spectral acceleration at the initial period of a given structure, $Sa(T_1,5\%)$, has been employed as the chosen IM (ASCE 7–05 2005). This is an ordinate on the elastic spectrum for a particular hazard level in terms of the annual frequency of exceedance, which can be obtained using conventional PSHA. The spectral accelerations are then plotted against the structural period, resulting in a UHS. Every ordinate in a UHS has an equal chance of being exceeded. Ground motions from small close-by earthquakes generally contribute most to the short-period range of a UHS, while large distant earthquakes contribute most in the long-period range (McGuire 1995).

Most examples in the literature on UHS and seismic disaggregation are based on the conventional (time-independent) PSHA. However, time-dependent PSHA has gained remarkable attention in recent years, especially during major earthquake sequences. Nevertheless, to our knowledge, there are no examples in the literature on the variation of UHS and the associated dominant scenarios (obtained from seismic disaggregation) during an ongoing sequence. Therefore, in the following, we present examples of these products using a short-term (daily) time-dependent seismic hazard model (Azarbakht et al. 2022). The input data and selected study site are discussed in the next section. Subsequently, the methodology for time-dependent PSHA is discussed. Finally, results and a discussion are presented.

2 Input data and selected sequences

The study area is the part of western Greece defined by 20-23E and 37-39 N, with a grid size of 0.05×0.05 degrees, which is the same as the 2013 European Seismic Hazard Model (ESHM13) (Giardini et al. 2013; Woessner et al. 2015). This choice of grid size makes it easier to include the background seismicity in the PSHA. This study considers the available technical literature on the earthquake sequences that occurred in this area (e.g. Karakostas et al., 2020). Patras, located in the study area, is Greece's third-most populated city and has several important facilities, including a large port. In addition, this city features numerous public buildings, schools, and historical landmarks. The Rio–Antirrio bridge spans the Gulf of Corinth near Patras. This is one of the world's longest multi-span cable-stayed bridges. Aegio, a town also in the study area, is known for a topographic plateau spanning a large fault (the cause of a destructive earthquake on 15 October 1995). This study area is chosen as it is in one of Europe's highest seismicity regions, where numerous earthquake sequences have occurred in the past decades. Because of this high seismicity, it is a testbed of the TURNkey project.[1]

The current study analyses two seismic sequences that occurred in the period from 1995 to 2018 whose mainshocks had moment magnitudes, Mw, greater than 6. The earthquake catalogue of the International Seismological Centre (ISC, last accessed 2020, Bondár and

---

[1] Towards more Earthquake-resilient Urban Societies through a Multi-sensor-based Information System enabling Earthquake Forecasting, Early Warning and Rapid Response actions (https://earthquake-turnkey.eu/).

Table 1 The selected sequences with mainshock magnitude Mw ≥ 6, mainshock occurrence time, and the distances to Patras and Aegio

Sequence Label	Lat. (N)	Lon. (E)	Mainshock Magnitude (Mw)	Mainshock Date (dd/mm/ yyyy)	Hour:Minute	Distance to Patras (km)	Distance to Aegio (km)
A	38.39	22.28	6.5	15/06/1995	00:15	50	23
F	37.53	20.62	6.8	25/10/2018	22:54	126	151

Storchak 2011) was employed for this study. Table 1 summarises the two sequences that are considered representative samples for this study area. The same lettering scheme as in Azarbakht et al. (2022) is used to avoid confusion for readers. Additionally, the spatial distribution of aftershock events, during one month after the mainshock origin time, are shown in Fig. 1 for the two considered sequences. Table 1 also indicates the distances between the epicentre of each mainshock and two key locations (Patras and Aegio) (sequence A is the closest to both Patras and Aegio). As shown in the following sections, the differences in sequence-to-site distance have a strong impact on the seismic hazard estimated at the two locations.

3 Methodology

OEF is always based on estimating time-dependent probabilities of potentially damaging earthquakes (Jordan et al. 2014). Its output is frequently expressed in terms of probability changes due to time-dependent (days to months) seismicity. These probabilities can be used by emergency managers as well as for public communication (Jordan and Jones 2010; Goltz 2015; Roeloffs and Goltz 2017; McBride et al. 2020; Field and Minler 2018; Douglas and Azarbakht 2021; Azarbakht et al. 2021).

The current study uses time-dependent PSHA (Azarbakht et al. 2022) to look at how UHS and the corresponding disaggregated seismic scenarios change during aftershock sequences. To forecast the frequency of occurrences over the aftershock zone within the required time span, the PSHA takes into account short-term changes in seismicity revealed by a Bayesian ETAS model (Azarbakht et al. 2022; Ebrahimian and Jalayer 2017). The seismicity in terms of the anticipated number of occurrences in the forecasting time interval (24 h) is employed as the short-term seismicity rate. As a result, a standard PSHA was undertaken initially, using Eq. (2) (derived and adapted from Cornell 1968; McGuire 1995; and numerically integrated over the aftershock zone, see also Eq. (1)):

$$\lambda(PGA > pga) = \lambda\big(M > M_{\min}\big) \int_{M_{\min}}^{M_{\max}} \int_{X_{\min}}^{X_{\max}} \int_{Y_{\min}}^{Y_{\max}} P\big(PGA > pga | m, d\{(x,y),(x_s,y_s)\}\big). \tag{2}$$
$$f_M(m).f_{X,Y}(x,y)dydxdm$$

where $\lambda(PGA > pga)$ is the annual rate of exceedance of *PGA* above a threshold *pga*; M_{min} is equal to 4.5 (the same assumption as in ESHM13); M_{max} is the maximum magnitude obtained from the ESHM13 results for each area source; $\lambda\big(M > M_{min}\big)$ is the annual rate of exceedance of earthquakes greater than M_{min}, which is numerically defined for each
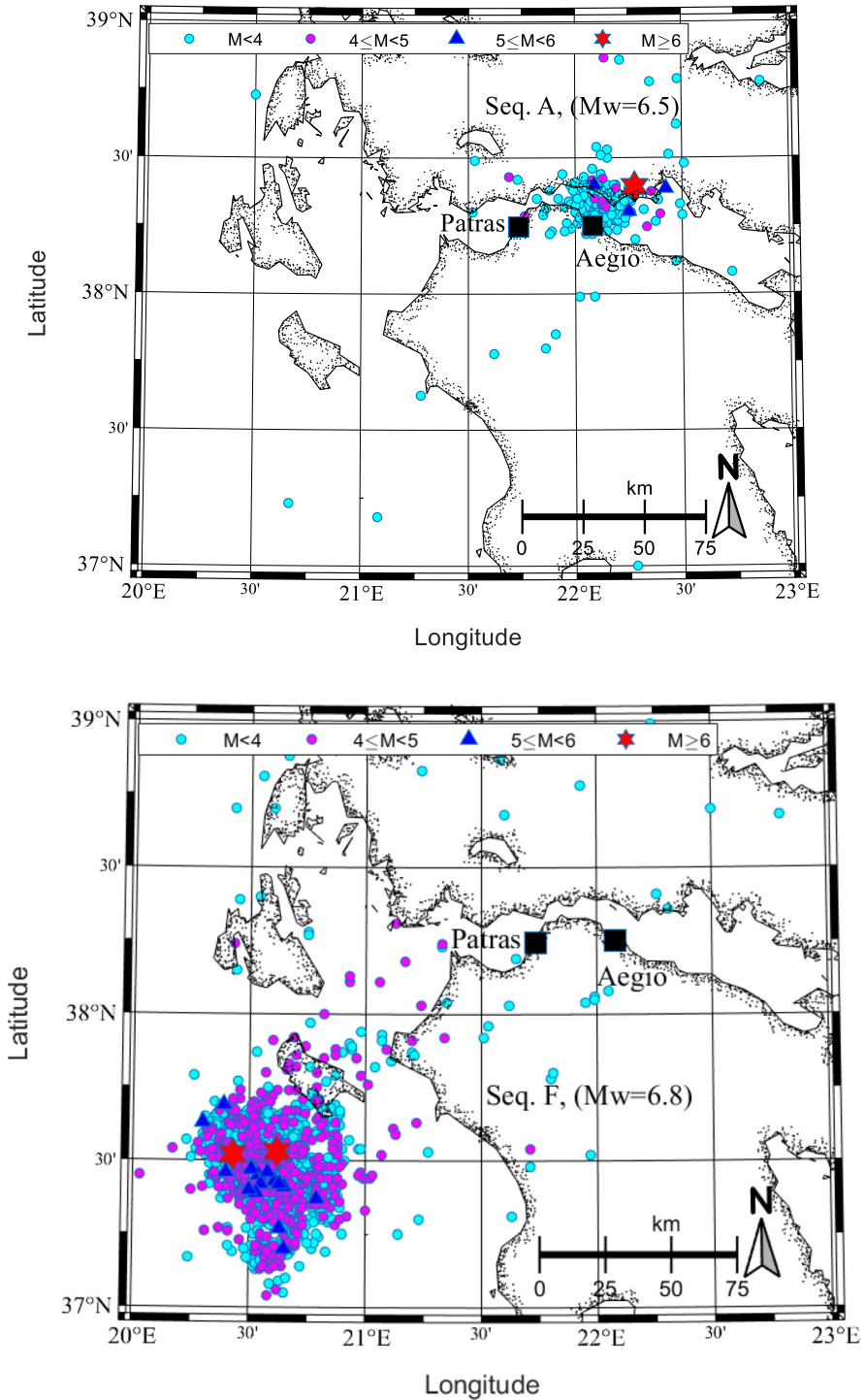
Fig. 1 The spatial distribution of aftershocks during one month after the mainshock for: (top) sequence A and (bottom) sequence F

grid cell based on the ESHM13 SEIFA model; $d\{(x,y),(x_s,y_s)\}$ is the epicentral distance between the desired site (x_s and y_s are the coordinates of the site of interest) and an arbitrary point (x and y coordinates $\in$ **A**) inside the aftershock zone (see also Ebrahimian et al. 2019); $P\big(PGA > pga|m,d\{(x,y),(x_s,y_s)\}\big)$ is the conditional probability of *PGA* exceeding a threshold *pga*, given a magnitude *m* and an epicentral distance *d* at the ($x,y \in$ **A**) coordinate, which can be estimated using a set of GMPEs; $f_M(m)$ is the probability density function of magnitude, which follows the Gutenberg-Richter relationship based on the ESHM13 for each area source; $f_{X,Y}(x,y)$ is the joint probability density function of the distance distribution at an arbitrary point with ($x,y \in$ **A**) from the site (x_s,y_s) coordinate, which has a uniform distribution, i.e. assuming equiprobable occurrence of earthquakes in the area source; X_{min} and X_{max} are, respectively, the lower and upper limits in the x-axis direction in Cartesian coordinates inside the study area ($\in$ **A**); Y_{min} and Y_{max} are, respectively, the lower and upper limits in the y-axis direction in Cartesian coordinates inside the study area ($\in$ **A**).

The issue of selecting GMPEs for PSHA has always been challenging (e.g. Danciu and Tselentis, 2007; Delavaud et al. 2012; Skarlatoudis et al. 2013). For simplicity, the Zhao et al. (2006) model is the only GMPE employed in this study to approximate the assumptions of ESHM13. We acknowledge that the impact of GMPE selection on the final short-term time-dependent PSHA is an interesting topic for future investigation but it is outside the scope of this study.

The short-term (daily) time-dependent PSHA is performed by substituting the rate $\lambda(M > M_{min})$ in Eq. (2) by the forecasted number of events obtained from the robust seismicity framework (e.g. that corresponding to sequence A) and over the forecasting time interval (24 h in the present study). The other parameters have the same definitions and values as those used for the background (time-independent) hazard calculations [see also Azarbakht et al. (2022)].

It is worth emphasising that the employed robust seismicity forecasting model (Ebrahimian and Jalayer 2017) has the crucial feature of combining Bayesian inference with a sophisticated simulation technique [namely, Markov Chain Monte Carlo (MCMC)] to update the ETAS model parameters. This framework enables different sources of uncertainty to be considered, i.e., the uncertainties in the ETAS model parameters and the variations in the sequence of events that may happen during the forecasting interval. This forecasting framework explicitly takes into account two sources of uncertainty: (1) the uncertainty in the ETAS model parameters conditional on the catalogue of observed events that are available prior to the forecasting interval's origin time, and (2) the uncertainty in the simulated sequence of events during the forecasting time interval. The results of this framework include the mean and confidence interval for the estimated number of occurrences, corresponding to a specific forecasting interval, as well as the spatial distribution of the anticipated events (as will be discussed in Fig. 2).

It is important to note that epistemic uncertainty in the hazard calculations is generally taken into account by employing several GMPEs and a sophisticated logic-tree, in addition to other uncertainties that are considered in the adopted framework, such as Bayesian inference and MCMC simulations in the ETAS forecasting model. A simple logic-tree has been chosen in the current study, however, because rapid computation is an important requirement for generating useful OEF products. Future studies could determine a more appropriate logic-tree for this region. Also, future research should
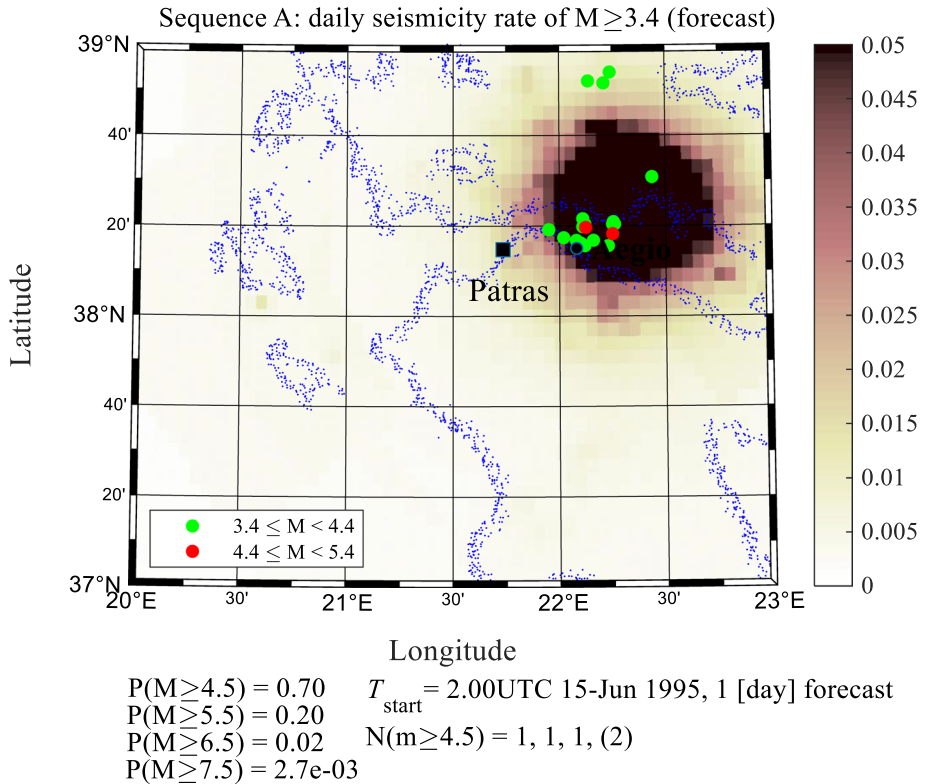
Fig. 2 The spatial distribution of the seismicity (the map reports the mean+2σ confidence interval, i.e. 98th percentile, for the number of events per km²) in the aftershock zone for 15 June 1995 (sequence A in Table1). The forecast interval is 24 h, starting from 02:00 UTC. The probability of having a magnitude greater than or equal to a given magnitude is shown in the figure's bottom-left corner. The forecasted numbers of events with $M \geq 4.5$ are shown in the bottom-right corner. The first, second, and third numbers indicate the 50th, 84th and 98th percentiles. The fourth number (in the parenthesis) indicates the observed number of events

focus on taking into account uncertainties from other sources, including the PSHA and forecasting algorithms.

4 Results and discussion

As previously stated, the seismicity forecasting model developed by Azarbakht et al. (2022) has been used to undertake time-dependent PSHA in this investigation. In the case of sequence A, T_{start} is set at 02:00 UTC, and the prediction interval is one day (24 h). T_{start} is almost an hour and 45 min after the sequence's mainshock (see Table 1) to obtain enough aftershock events following the mainshock and properly adapt the forecasting model to the characteristics of the sequence. The mainshock of Sequence A had a magnitude of 6.5 and occurred towards the northeast corner of the considered aftershock zone, at 38.39 N and 22.28E.

Figure 2 depicts the anticipated short-term spatial distribution of seismicity in the study area in terms of the mean plus 2σ (98 per cent confidence interval) over the forecast time-frame of one day (24 h) following T_{start} of 02:00 UTC on 15 June 1995. The observed earthquakes that occurred during the associated predicted interval are also shown. The colour bar in Fig. 2 depicts the expected frequency of occurrences (per day and per km^2) of events of magnitude $\geq M_l$ (in this case, $M_l = M_c = 3.4$). M_c is computed (Wiemer 2001) using the sequence of events. The epicentral zone is expected to show increased seismicity, as indicated in Fig. 2.

In the bottom-left corner of Fig. 2, the probabilities of exceeding various magnitude thresholds (ranging from 4.5 to 7.5) are depicted. Since the greatest magnitude in ESHM13 (Giardini et al. 2013; Woessner et al. 2015) for all the area sources in the study region is between 7.2 and 8.1, the upper limit for the magnitude is assumed to be 7.5 for simplicity (for details see Azarbakht et al. 2022). The probabilities displayed at the bottom of Fig. 2 apply to an event occurring anywhere within the study area and should not be regarded as a prediction of a specific occurrence at a specific location. The combination of anticipated numbers over all cells yields these probabilities. For example, the probability of experiencing Mw ≥ 4.5 on the first day after a mainshock anywhere in the study area is 0.70. This forecast is plausible because only two Mw ≥ 4.5 occurrences were observed in this time span (Fig. 2), and can be compared to the forecasted number of events, which is one in this case.

Figure 2 shows the forecasted number of events within the aftershock zone with Mw ≥ 4.5 (the minimum magnitude assumed in ESHM13 for seismic hazard calculations). The forecasted 50th percentile (the median value, equivalent to the logarithmic mean in an arithmetic scale), the 84th percentile (logarithmic mean plus one logarithmic σ in an arithmetic scale), and the 98th percentile (logarithmic mean plus two logarithmic σ in an arithmetic scale) are indicated by the first, second, and third numbers, respectively (all are one in this case). The fourth number (within the parenthesis) represents the number of events observed (two in this case). The forecasted numbers of events are in good agreement with the observed data, as shown in Fig. 2. This is a built-in criterion for evaluating the forecasting algorithm's quality. It is worth noting that the forecasted number of events is calculated as a real number, but it is rounded to the nearest integer. As a result, as seen in Fig. 2, several percentiles for a given time interval are the same.

As the forecasted and observed number of events are in good agreement for both considered sequences in Table 1 (as well as four other sequences previously studied), we rely on this short-term seismicity model and conduct a time-dependent PSHA (Azarbakht et al 2022) on this basis to assess the UHS and hazard disaggregation. The results for Patras of the conventional and time-dependent PSHA are displayed in Fig. 4 which shows the daily probability of exceedance on the left and the daily rate of exceedance on the right. Then, to account for the summation of background seismicity (from conventional PSHA) and short-term seismicity, $\lambda(M > M_{min})$ is altered with the expected number of occurrences within the forecasting interval (herein, one day) arising from the implemented seismicity forecasting framework. Based on this enhanced short-term seismicity, the hazard integral (Eq. 2) is recalculated. Figure 3 shows the results of this time-dependent PSHA for Patras on 15 June 1995, in the left (median daily probability of exceedance) and the right (median daily rate of exceedance) panels. It is worth mentioning that the occurrence of earthquakes of interest is considered to be modelled by a Poisson process. Hence, the annual frequency of exceedance generated from the long-term (time-independent) hazard is converted to the daily rate (by dividing by 365) and then transformed into the daily probability of exceedance using the
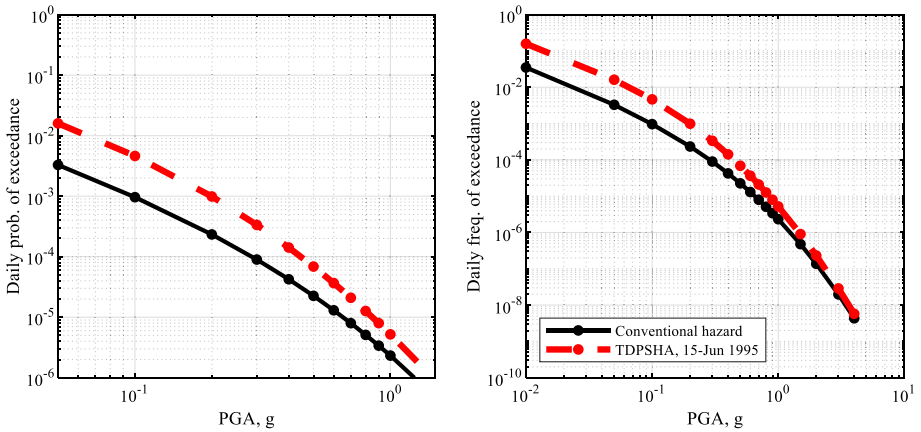
Fig. 3 Short-term PSHA for Patras for 15 June 1995 (sequence A in Table 1) and the forecast interval equal to 24 h, and starting time from 02:00 UTC, (left): the short-term time-dependent daily probability of exceedance versus *PGA* and comparison with the conventional daily hazard curve, and, (right): short-term time-dependent daily rate of exceedance versus *PGA* and comparison with the conventional daily hazard curve
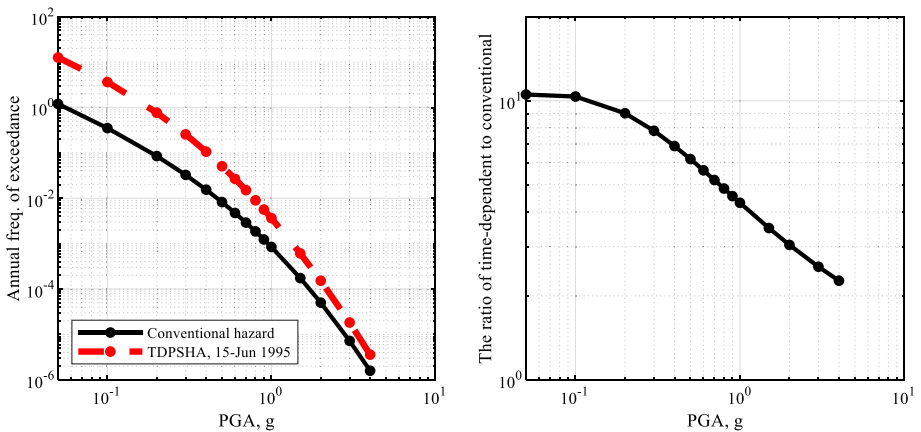
Fig. 4 (left): short-term versus conventional annual frequency of exceedance versus *PGA* for Patras for 15 June 1995 (sequence A in Table 1) and based on the forecast interval equal to 24 h, and starting time from 02:00 UTC, (right): the ratio of the short-term time-dependent annual frequency of exceedance (red curve in the left subplot) over the conventional annual frequency of exceedance (black curve in the left subplot) versus *PGA*

Poisson distribution for comparison with standard PSHA. Because short-term seismicity during aftershock sequences can only enhance long-term hazard, the conventional hazard curve represents a lower bound for this short-term hazard curve. It is worth noting that, as seen in Fig. 3, the time-dependent hazard approaches the conventional hazard at high levels of PGA. This is because the largest difference between these two curves occurs at short hazard values due to the ongoing seismic sequence. That is why the focus of the present study is on short-term hazard levels, which are of great interest
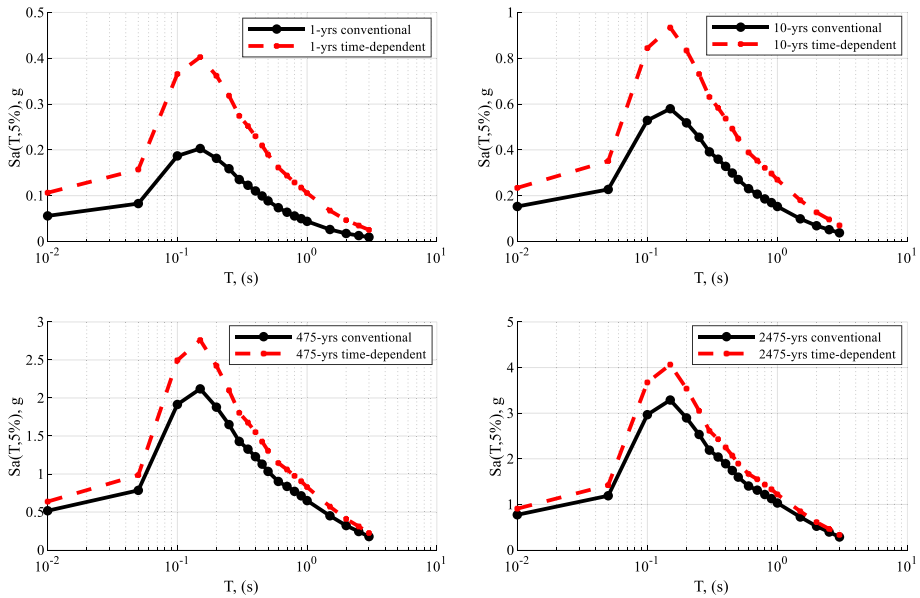
Fig. 5 The long-term UHS (solid-line) and the short-term UHS (red dashed line), based on the 24-h forecast on 15 June 1995 at 02:00 UTC, sequence A in Table 1, (top-left): 9 9.$\bar{9}$ per cent probability in 50 years equal to 1-year return period, (top-right): 99.5 per cent probability in 50 years equal to 10-year return period, (bottom-left): 10 per cent probability in 50 years equal to 475-year return period, (bottom-right): 2 per cent probability in 50 years equal to 2475-year return period

for first responders during an earthquake sequence. To better elaborate on this phenomenon we were inspired by McGuire (2012) to assess the statistical significance of the results. McGuire (2012) concludes that if a seismic hazard study uses an alternative assumption or parameter and it changes the calculated mean hazard by less than 25% for ground motions corresponding to 10^{-4} annual frequency of exceedance, and by less than 35% for ground motions corresponding to 10^{-6} annual frequency of exceedance, then that potential change is less than the best level of confidence possibleTherefore, the change might be considered negligible. Therefore we illustrate the time-dependent and the conventional annual frequency of exceedance in Fig. 4 (left) and the corresponding ratio of the two curves in Fig. 4 (right). As can be seen in Fig. 4 (right), the ratio of time-dependent hazard over the conventional one is always more than two even at very large return periods (small annual frequenues of exceedance). Hence, we can conclude that the short-term hazard is statistically significant, especially in the days following the mainshock.This statistical significance decays with time.

The UHS curves for four return periods are shown in Fig. 5. The one-year return period (9 9.$\bar{9}$ per cent probability in 50 years) is chosen to represent a rational short timeframe of potential interest for emergency first responders. Infrastructures' serviceability criteria are usually associated with an event with a ten-year return period (99.5 per cent probability in 50 years). The 475- and 2475-year return periods (10 and 2 per cent probability in 50 years, respectively) are also plotted here. These are the most common seismic hazard levels for the design of infrastructures corresponding to limit states of, e.g., immediate occupancy, life safety and collapse prevention. In Fig. 5 the solid
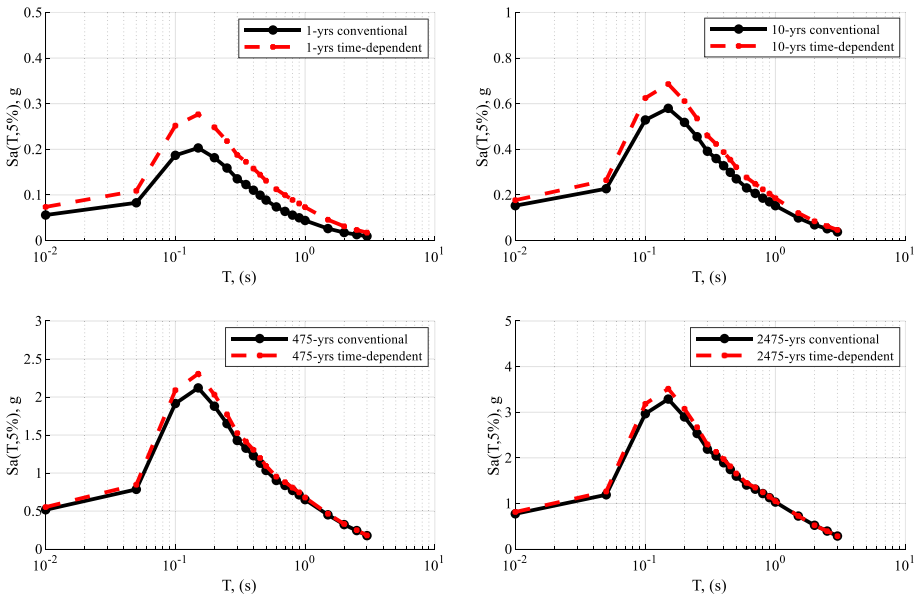
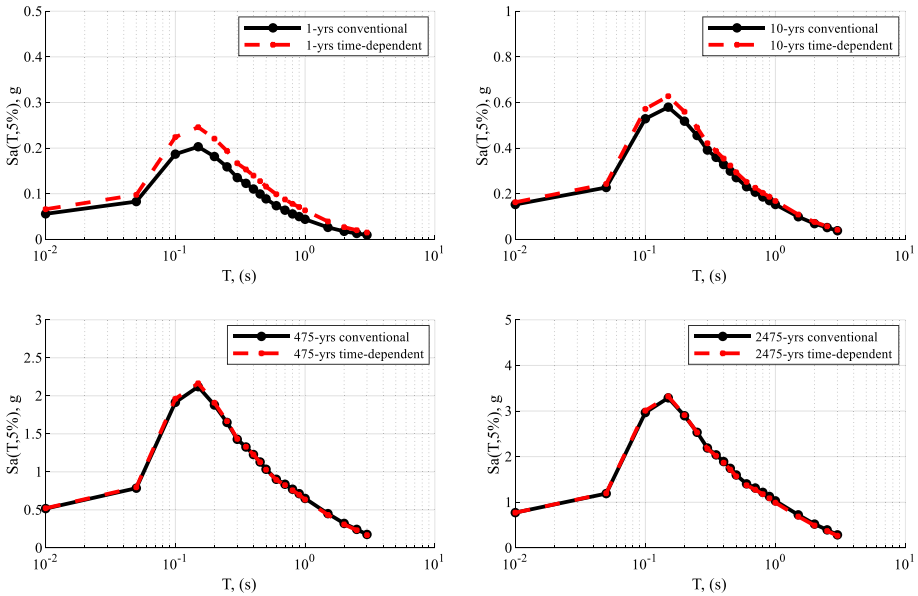**Fig. 6** As for Fig. 5 but for sequence F in Table 1 on 26 October 2018 at 00:00 UTC

Fig. 7 As for Fig. 5 but for sequence F in Table 1 on 29 October 2018 at 00:00 UTC

black line represents time-independent (conventional) UHS and the dashed red line shows the time-dependent UHS. The shortest return period shows the highest difference between the two UHS. It is worth mentioning that all the cases in Fig. 5 are for the 24-h
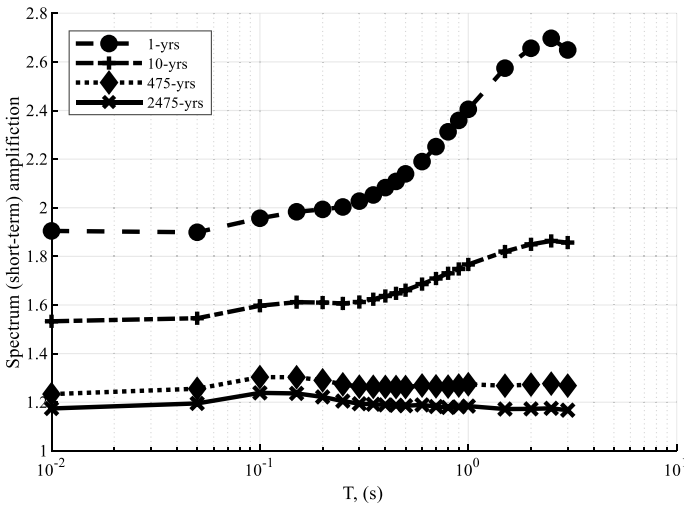
Fig. 8 The ratio of time-dependent UHS over time-invariant (conventional) UHS (see Fig. 5) in Patras for a 24-h forecast on 15 June 1995 at 02:00 UTC for different UHS cases corresponding to four return periods (sequence A in Table 1)

forecast following the mainshock in sequence A. The same information for sequence F (the most recent large earthquake in the study area) is shown in Figs. 6 and 7, respectively, for 26 and 29 October 2018. By comparing Figs. 6 and 7, it can be inferred that the time-dependent UHS have decayed with time. Hence, we can imagine that the difference between time-dependent and conventional UHS gets lower as time passes. The period of heightened hazard only lasts a few hours/days following a mainshock. Therefore, the speed of any OEF platform and the speed of the first responder's decisions are vital in the first golden hours following a severe mainshock. Besides, by comparing Figs. 5 and 6, it is revealed that the mainshock's distance to the site is a key parameter influencing the UHS. The sequences A and F are, respectively, 50 km and 126 km from Patras. The heightened seismic hazard, as seen in Figs. 5 and 6, is more significant for sequence A, which is nearer.

To demonstrate this observation more clearly, the ratio of time-dependent UHS to the time-invariant UHS, here called "spectrum amplification", based on Fig. 5 is shown in Fig. 8 for different return periods. As seen in Fig. 8, the time-dependent seismicity has the most influence at long structural periods, i.e. it reaches almost 1.7 and 2.4 in the cases of 10- and 1-year return periods, respectively, for structural periods greater than 1 s. The spectrum amplification is almost the same for 475 and 2475-year return period cases and around 1.1 to 1.2 for all structural periods. The spectrum amplification approaches unity when enough time passes after the mainshock origin time.

Seismic disaggregation, illustrated in Figs. 9, 10 and 11 is another important product of PSHA. In Figs. 9, 10 and 11 the left column is for conventional PSHA and the right column is for time-dependent PSHA. All plots are for a 24-h forecast following the mainshock, Fig. 9 is for sequence A on 15 June 1995 at 02:00 UTC, Fig. 10 is for sequence F on 26 October 2018 at 00:00 UTC, and Fig. 11 is for sequence F on 29 October 2018 at 00:00 UTC (see Table 1). In the top subplots, the horizontal axes are the moment magnitude and the distance between Patras (38.24E and 21.73 N) and the mainshock's epicentre. The
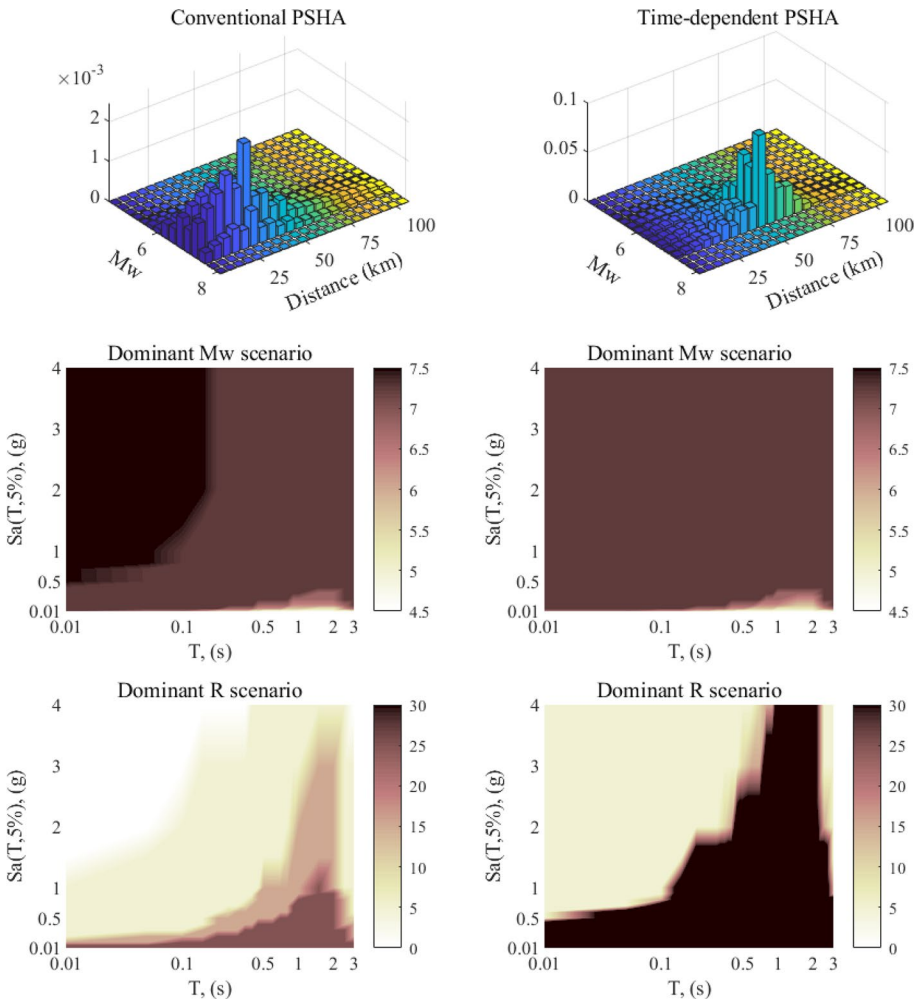
Fig. 9 The left column figures represent time-independent results and the right column figures correspond to the time-dependent case in Patras for a 24-h forecast on 15 June 1995 at 02:00 UTC (sequence A in Table 1). Top figure: seismic disaggregation of hazard corresponding to $Sa(T=1,5\%)=0.1$ g, middle figure: dominant moment magnitude scenarios for all disaggregation cases, bottom figure: dominant distance scenarios for all disaggregation cases

vertical axis represents the contribution of each (M, R) pair to the total hazard. Therefore, the peak in this subplot is considered the dominant scenario (see also Ebrahimian et al. 2012) as its contribution to the hazard is more significant than the other combinations of (M, R). As an example, as seen in Fig. 9 top subplot figures, the dominant scenario has shifted to the farthest distance, and also multiple peaks can be seen in the time-dependent case. In other words, the forecasted dominant scenario for the next 24 h following the mainshock contains wider magnitudes at a farther distance when compared to the long-term seismic hazard. However, by comparison of the two top subplots in Figs. 10 and 11, it is inferred that the dominant scenario has stayed almost the same in terms of distance
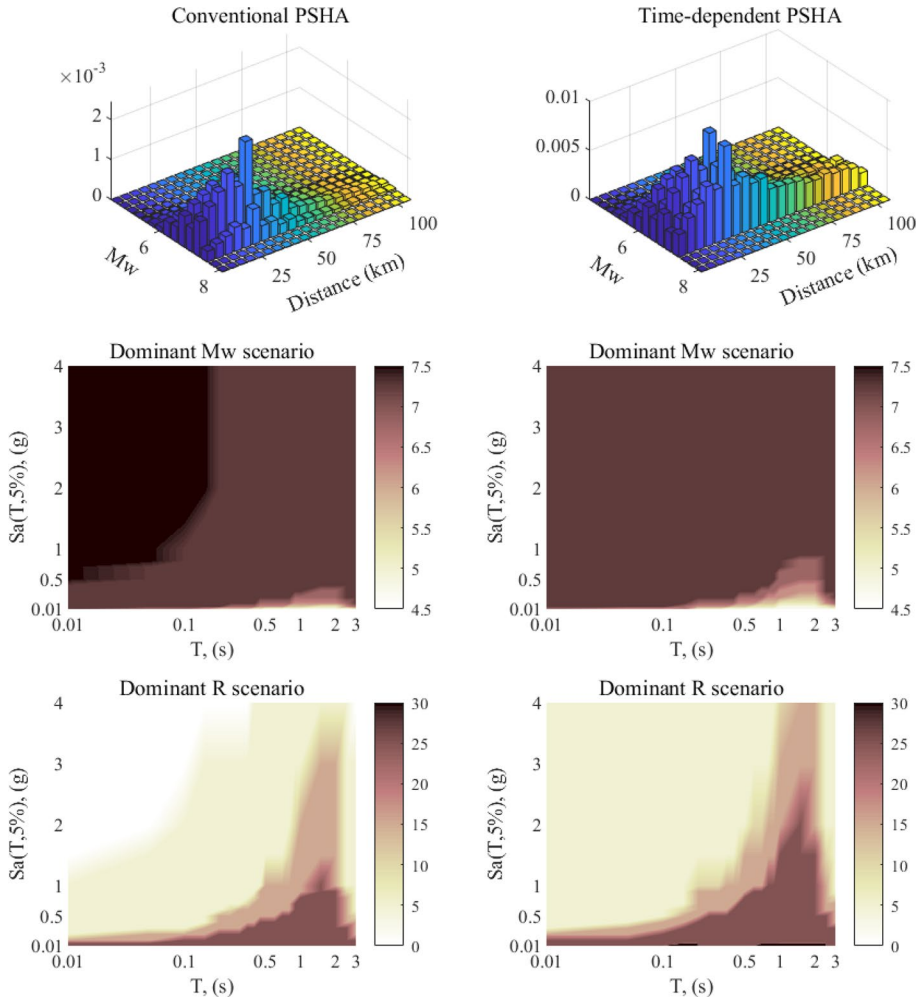
Fig. 10 As for Fig. 9 but for sequence F in Table 1 on 26 October 2018 at 00:00 UTC

between the background and time-dependent hazard. Additionally, in all three cases, the forecasted dominant magnitude has a lower contribution (more peaks can be seen) than the dominant magnitude in the background seismic hazard. However, large (Mw ~ 6.5) earthquakes at moderate distances (~ 50–100 km) contribute more to the time-dependent hazard. This is because the mainshock in sequence F is 126 km from Patras (see Table 1).

As previously described, the disaggregation results, as well as the corresponding dominant scenario, are associated with a given point on the hazard curve. Therefore, this procedure is repeated for all the considered points on the hazard curves for different structural periods. The obtained results for magnitude are shown in the middle subplots in Figs. 9, 10 and 11, in which the left subplot is for conventional PSHA and the right subplot is for time-dependent PSHA. Additionally, the obtained results for distance are provided in the bottom subplots in Figs. 9, 10 and 11, in which the left subplot is for conventional PSHA and the right subplot is for time-dependent PSHA. As seen in Figs. 9, 10 and 11 middle and bottom
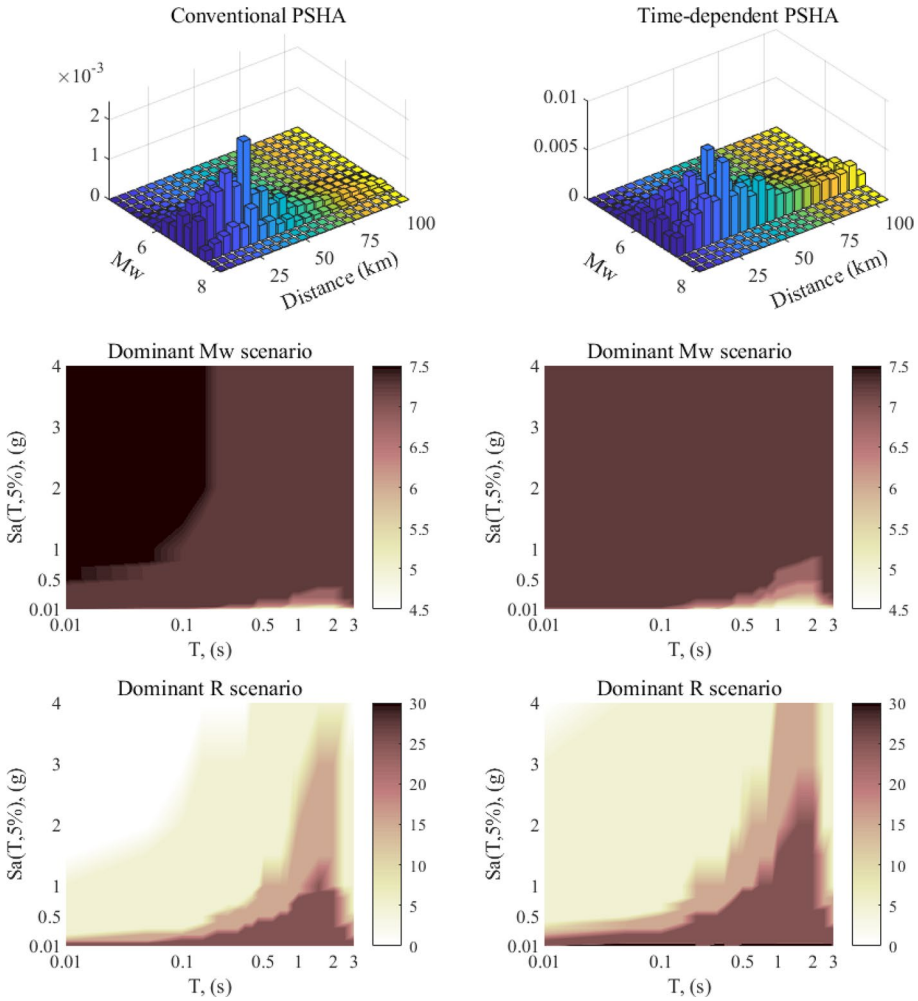
Fig. 11 As for Fig. 9 but for sequence F in Table 1 on 29 October 2018 at 00:00 UTC

graphs, the x-axis is the structural period and the y-axis corresponds to the $Sa(T_1,5\%)$ at which the associated hazard curve has been disaggregated. In other words, low $Sa(T_1,5\%)$ values represent high probabilities of exceedance over the lifetime of a given infrastructure (long return periods) and vice versa. As seen in the middle graphs in Figs. 9, 10 and 11 a comparison of the short-term and conventional hazard reveals that based on the short-term (time-dependent) hazard the chance of moderate magnitude events contributing to long structural periods and low return periods has increased. Additionally, the chance of large magnitude events contributing to short structural periods and long return periods has decreased. In other words, the chance of having a large event after a severe mainshock is low. The same comparison can be made between the bottom subplots which represent the dominant distance scenarios. The distant events for long structural periods at short return periods have increased when we compare the bottom subplots in Figs. 10 and 11. However,

this chance is significantly increased in Fig. 9 (bottom subplot figures) for all structural periods, especially for short return periods.

Overall, the chance of large earthquakes (Mw 6–7) at around 25 km has increased, which mostly affects long structural periods at short return periods. This graphical representation summarises all the disaggregation results in a single figure, which is a useful complement to UHS. This novel presentation facilitates the end-user's understanding of forecasted dominant scenarios for the next 24 h. Hence, it can be useful within a multi-disciplinary decision-making process as part of an earthquake risk management platform.

5 Conclusions

A time-dependent seismic hazard model has been implemented for western Greece, one of the most seismic prone regions in Europe. Two recent seismic sequences (from 1995 and 2018) were selected to be retrospectively investigated in order to compare the results of time-invariant and time-dependent seismic hazard assessments. Uniform hazard spectra and disaggregated seismic scenarios were chosen as two outcomes of PSHA that are useful for engineering. The variation in uniform hazard spectra and the dominant seismic scenarios were assessed directly after each mainshock and also a few days after the mainshock. For this purpose, four return periods were considered to cover different engineering interests: short-term hazard variation for first responders, mid-term variations for serviceability and long-term variations for design. The results revealed that the short-term increase in the spectra is more significant at short return periods and for long structural periods. This increase decays rapidly with time since the mainshock.

The disaggregation results are presented in a novel manner to enable interpretation of the possible dominant scenario by means of magnitude, distance, structural period and ground-motion level. The proposed disaggregation presentation enables end-users (e.g. decision-makers) to compare the forecasted dominant earthquake scenarios from the background and the time-variant seismic hazard model during a period of heightened seismic hazard.

The results of this study can be used in regions with a high potential for aftershocks. The short-term hazard variations may be useful for first responders when developing search and rescue plans. They may also be relevant for industrial facilities when deciding whether to continue or restart their operations during seismic sequences. The mid- and long-term results could be compared to conventional hazard models to help understand how the engineering demand structures might experience during a severe seismic sequence varies with time. In addition, the results may of interest when assessing the earthquake response of structures for which cumulative damage plays an important role as a seismic sequence may impose un-predicted engineering demand and hence unexpected damage to the structure. Finally, seismic codes could use these models to assess the potential impact of heightened hazard when designing critical infrastructure.

Societies through a Multi-sensor-based Information System enabling Earthquake Forecasting, Early Warning and Rapid Response actions).

Data availability Earthquake catalogue data were provided by ISC (last accessed 2020).

Declarations

Conflict of interest The authors have no relevant financial or non-financial interests to disclose.

Open Access This article is licensed under a Creative Commons Attribution 4.0 International License, which permits use, sharing, adaptation, distribution and reproduction in any medium or format, as long as you give appropriate credit to the original author(s) and the source, provide a link to the Creative Commons licence, and indicate if changes were made. The images or other third party material in this article are included in the article's Creative Commons licence, unless indicated otherwise in a credit line to the material. If material is not included in the article's Creative Commons licence and your intended use is not permitted by statutory regulation or exceeds the permitted use, you will need to obtain permission directly from the copyright holder. To view a copy of this licence, visit http://creativecommons.org/licenses/by/4.0/.

References

ASCE7-5 (2005) Minimum Design Loads for Buildings and Other Structures, American Society of Civil Engineers/Structural Engineering Institute, Reston, VA

Azarbakht A, Rudman A, Douglas J (2021) A decision-making approach for operational earthquake forecasting. Int J Disaster Risk Reduct 66:1–13

Azarbakht A, Ebrahimian H, Jalayer F, Douglas J (2022) Variations in hazard during earthquake sequences between 1995 and 2018 in western Greece as revealed by a Bayesian ETAS model. Geophys J Int 231(1):27–46. https://doi.org/10.1093/gji/ggac177

Bazzurro P, Cornell CA (1999) Disaggregation of seismic hazard. Bull Seismol Soc Am 89(2):501–520

Bondár I, Storchak D (2011) Improved location procedures at the International Seismological Centre. Geophys J Int 186(3):1220–1244

CEN (2003) Eurocode 8 Design of structures for earthquake resistance. Part 1: general rules, seismic actions and rules for buildings Final draft prEN 1998. European Committee for Standardization, Brussels

Cornell CA (1968) Engineering seismic risk analysis. Bull Seismol Soc Am 58(5):1583–1606

Danciu L, Tselentis GA (2007) Engineering ground-motion parameters attenuation relationships for Greece. Bull Seismol Soc Am 97(1B):162–183

Delavaud E, Cotton F, Akkar S, Scherbaum F, Danciu L, Beauval C, Drouet S, Douglas J, Basili R, Sandikkaya MA, Segou M (2012) Toward a ground-motion logic tree for probabilistic seismic hazard assessment in Europe. J Seismolog 16(3):451–473

Douglas J, Azarbakht A (2021) Cost–benefit analyses to assess the potential of operational earthquake forecasting prior to a mainshock in Europe. Nat Hazards 105(1):293–311

Ebrahimian H, Jalayer F (2017) Robust seismicity forecasting based on Bayesian parameter estimation for epidemiological spatio-temporal aftershock clustering models. Sci Rep 7(1):1–15

Ebrahimian H, Azarbakht A, Tabandeh A, Golafshani AA (2012) The exact and approximate conditional spectra in the multi-seismic-sources regions. Soil Dyn Earthq Eng 39:61–77

Ebrahimian H, Jalayer F, Forte G, Convertito V, Licata V, d'Onofrio A, Santo A, Silvestri F, Manfredi G (2019) Site-specific probabilistic seismic hazard analysis for the western area of Naples. Italy Bull Earthq Eng 17(9):4743–4796

Field EH, Milner KR (2018) Candidate products for operational earthquake forecasting illustrated using the HayWired planning scenario, including one very quick (and not-so-dirty) hazard-map option. Seismol Res Lett 89(4):1420–1434

Gerstenberger MC, Wiemer S, Jones LM, Reasenberg PA (2005) Real-time forecasts of tomorrow's earthquakes in California. Nature 435(7040):328–331. https://doi.org/10.1038/nature03622

Giardini D, Woessner J, Danciu L, Crowley H, Cotton F, Grünthal G, Pinho R et al. (2013) Seismic Hazard Harmonisation in Europe (SHARE): Online Data Resource.doi: https://doi.org/10.12686/SED-00000001-SHARE

Goltz JD (2015) A further note on operational earthquake forecasting: an emergency management perspective. Bull Seismol Soc Am 86(5):1231–1233

Gulia L, Tormann T, Wiemer S, Herrmann M, Seif S (2016) Short-term probabilistic earthquake risk assessment considering time-dependent b values. Geophys Res Lett 43(3):1100–1108

International Seismological Centre (2020), On-line Bulletin, doi:https://doi.org/10.31905/D808B830

Jordan TH, Jones LM (2010) Operational earthquake forecasting: some thoughts on why and how. Seismol Res Lett 81(4):571–574

Jordan TH, Marzocchi W, Michael AJ, Gerstenberger MC (2014) Operational earthquake forecasting can enhance earthquake preparedness. Seismol Res Lett 85(5):955–959

Karakostas V, Kostoglou A, Chorozoglou D, Papadimitriou E (2020) Relocation of the 2018 Zakynthos, Greece, aftershock sequence: spatiotemporal analysis deciphering mechanism diversity and aftershock statistics. Acta Geophys 68(5):1263–1294

Marzocchi W, Iervolino I, Giorgio M, Falcone G (2015) When is the probability of a large earthquake too small? Seismol Res Lett 86(6):1674–1678

Marzocchi W, Taroni M, Falcone G (2017) Earthquake forecasting during the complex amatrice-norcia seismic sequence. Sci Adv 3(9):1–8. https://doi.org/10.1126/sciadv.1701239

McBride SK, Llenos AL, Page MT, Van Der Elst N (2020) EarthquakeAdvisory: exploring discourse between government officials, news media, and social media during the 2016 Bombay Beach Swarm. Seismol Res Lett 91(1):438–451

McGuire RK (1995) Probabilistic seismic hazard analysis and design earthquakes: closing the loop. Bull Seismol Soc Am 85(5):1275–1284

McGuire RK (2012). Precision of seismic hazard evaluations in central and eastern North America. In: Proceedings of 15th World Conference on Earthquake Engineering

Roeloffs E, Goltz J (2017) The California earthquake advisory plan: a history. Seismol Res Lett 88(3):784–797

Skarlatoudis AA, Papazachos CB, Margaris BN, Ventouzi C, Kalogeras I (2013) EGELADOS Group Ground-motion prediction equations of intermediate-depth earthquakes in the Hellenic arc, southern Aegean subduction area. Bull Seismol Soc Am 103(3):1952–1968

Wiemer S (2001) A software package to analyse seismicity: ZMAP. Seismol Res Lett 72(3):373–382

Woessner J, Laurentiu D, Giardini D, Crowley H, Cotton F, Grünthal G, Stucchi M (2015) The 2013 European seismic hazard model: key components and results. Bull Earthq Eng 13(12):3553–3596

Zhao JX, Zhang J, Asano A, Ohno Y, Oouchi T, Takahashi T, Fukushima Y (2006) Attenuation relations of strong ground motion in Japan using site classification based on predominant period. Bull Seismol Soc Am 96(3):898–913